In situ synchrotron X-ray diffraction study of the effect of microstructure and boundary layer conditions on CO2 corrosion of pipeline steels

Ko, M.; Ingham, B.; Laycock, N.; Williams, D.e.

DOI:
10.1016/j.corsci.2014.10.010

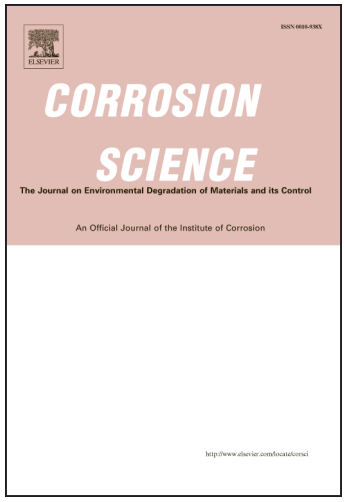

In situ synchrotron x-ray diffraction study of the effect of microstructure and boundary layer conditions on co_2 corrosion of pipeline steels

M. Ko, B. Ingham, N. Laycock, D.E. Williams

PII: S0010-938X(14)00467-3
DOI: http://dx.doi.org/10.1016/j.corsci.2014.10.010
Reference: CS 6040

To appear in: *Corrosion Science*

Received Date: 11 July 2014
Accepted Date: 10 October 2014

Please cite this article as: M. Ko, B. Ingham, N. Laycock, D.E. Williams, *In situ* synchrotron x-ray diffraction study of the effect of microstructure and boundary layer conditions on co_2 corrosion of pipeline steels, *Corrosion Science* (2014), doi: http://dx.doi.org/10.1016/j.corsci.2014.10.010

IN SITU SYNCHROTRON X-RAY DIFFRACTION STUDY OF THE EFFECT OF MICROSTRUCTURE AND BOUNDARY LAYER CONDITIONS ON CO_2 CORROSION OF PIPELINE STEELS

M. Ko[1,4], B. Ingham[2,5], N. Laycock[3] and D. E. Williams[4,5]

[1]Quest Integrity Group
PO Box 38-096, Lower Hutt 5045, New Zealand
m.ko@questintegrity.com
Phone: +64 4 978 6661, Fax: +64 4 978 9930

[2]Callaghan Innovation
PO Box 31-310, Lower Hutt 5010, New Zealand

[3]College of Engineering and Physical Sciences
University of Birmingham, UK

[4] School of Chemical Sciences, University of Auckland
Private Bag 92019, Auckland, 1022, New Zealand

[5]MacDiarmid Institute for Advanced Materials and Nanotechnology
School of Chemical and Physical Sciences, Victoria University of Wellington
P.O. Box 600, Wellington 6440, New Zealand

ABSTRACT

This study demonstrates that the nucleation of crystalline scales of siderite and chukanovite onto the surface of low-alloy steels under CO_2 corrosion at elevated temperature is critically dependent on initial surface roughness, on microstructure-related surface roughness developed during corrosion, and on stirring in the solution. This study confirms that effects due to chromium micro-alloying in the steel are extremely important for siderite nucleation. On average, these effects dominate over the effects of microstructure. However, spatial variation of the corrosion deposit thickness indicates an interdependence between microstructure and chromium-enhanced siderite nucleation with the possibility of localised corrosion developing as a result.

Keywords: A. low alloy steel; A. carbon steel; B. X-ray diffraction; B. potentiostatic

INTRODUCTION

Carbon dioxide (CO_2) corrosion has been a long-standing problem in the oil and gas production industry. The underlying mechanism of CO_2 corrosion is complex and influenced by a number of factors including environmental, physical and metallurgical variables. One of the methods to control CO_2 corrosion is to induce the formation of a protective corrosion product layer. This layer can provide a degree of protectiveness against CO_2 corrosion, by providing a physical barrier, restricting the diffusion of corrosive species into the steel surface and by blocking the steel surface from further corrosion. Conventional ex-situ measurements generally show that the corrosion product scales mainly comprise $FeCO_3$ (siderite), but that there is considerable variation in morphology, composition and protectiveness. Fe_3C (cementite), being the remains of the original steel microstructure, is also often observed to be incorporated within the formed layer, along with siderite [1, 2].

The formation of these corrosion products is known to be sensitive to the steel composition and microstructure as well as on the environmental factors such as CO_2 partial pressure, temperature, pH, and the presence and concentration of other ionic species in the solution. The steel microstructure and composition are interdependent variables and both have significant effects on corrosion processes. In particular, the size and distribution of cementite within the steel structure often determines the protectiveness of the formed layer [3, 4]. The roles of the cementite phase have been much discussed in the literature [1, 2, 5-9] and it can have either a beneficial or a detrimental effect on the formation of protective scales and the subsequent corrosion rate.

For example, some studies have shown steels with ferritic pearlitic microstructure to have improved CO_2 corrosion resistance, due to the distinct layering of ferrite and cementite phases in the pearlitic region [8-10]. It is well established that cementite is more cathodic than ferrite and the difference in potential between these two phases results in microgalvanic selective attacks of the ferrite phase at and around the pearlite bands [5, 11, 12]. Under certain conditions, the cementite platelets can provide an enclosed environment with stagnant flow conditions allowing for Fe^{2+} accumulation, and promoting precipitation of a well adhered corrosion product. This 'anchoring' effect around the pearlite region generally results in a homogeneous layer with better localised corrosion resistance [7-9]. Martensitic steels, with a dispersed cementite phase, often have poorly adherent corrosion products which lead to severe localised corrosion at temperatures below 80°C [7, 8]. Paolinelli et al. [10, 13] conducted polarisation tests on both ferritic pearlitic and quenched and tempered steel samples and reported a 20% lower corrosion rate for the ferritic pearlitic sample.

However, surface morphology analysis showed that both samples exhibited homogeneous and compact corrosion product layers with no indication of localised corrosion.

However, contradictory results to these have been reported both in laboratory studies and in field experience. Al-Hassan et al. [14] reported that ferritic pearlitic steels can have varying corrosion rates depending on the heat treatment, for example: ferritic pearlitic steel sample in the as-received state (thermo-mechanically processed) had a much higher corrosion rate compared to the same microstructure in the annealed state. They also reported a reduction of the corrosion rate due to the formation of iron hydroxycarbonate at temperatures above 60°C. However, the significance of this hydroxyl phase is not well understood. A study by Stegmann et al. and reported by Lopez et al. [4] showed that quenched and tempered steels with a needle-like carbide phase provides a better anchoring effect for corrosion product scales than that obtained for steels with larger ferrite area and few pearlite grains. Dugstad et al. [15] have also reported higher corrosion rates on ferritic pearlitic and spheroidised steel compared to that on steel with a quenched and tempered microstructure. Some researchers have proposed that in some cases, accumulation of the carbide layer causes further corrosion and surface acidification, preventing siderite precipitation and thus additionally increasing the corrosion rate [5, 6]. Gulbrandsen et al. [16] have reported a detrimental effect of a cementite layer on corrosion inhibitor effectiveness, in agreement with Paolinelli et al. [10] that showed improved inhibitor performance on quenched and tempered samples under most experimental conditions tested.

The addition of chromium as a minor alloying element generally improves the corrosion resistance of carbon steel in CO_2 environments and this effect is generally attributed to formation of a chromium enriched protective scale [14, 17-19]. However, the role of microstructure is not completely clear. Al-Hassan et al. [14] reported that for chromium containing steels, a quenched and tempered sample provided better corrosion resistance compared to an annealed sample. They proposed that the addition of alloying elements such as chromium can greatly reduce the corrosion rate by preventing the formation of a cementite layer. Dugstad et al. [15] observed the formation of protective corrosion scales on all heat treated chromium containing steels. They speculated that the presence of alloying element, rather than the metal microstructure is the determining factor for protection.

It is generally accepted that corrosion rates in a CO_2 environment are highly dependent on the protectiveness of the scale, which in turn depends on the nature of the base alloy (composition and microstructure) and on the environment (temperature, CO_2 partial pressure, pH) [1, 20-25]. These understanding are captured in various models that have

been developed in the oil and gas industry to predict the CO_2 corrosion rate for expected service conditions. These models are reviewed extensively in [26, 27]. However, there is a lack of understanding on the interaction between the material and environmental effects on the parameters of nucleation, growth and morphology of the formed scales. Our recent work using *in situ* synchrotron techniques has explored the mechanism behind the nucleation and growth of such protective scales at 80°C and in the presence of solution additives [28-30]. This work showed the importance of the development of boundary layer conditions within which a critical supersaturation required for siderite precipitation could be achieved. The kinetics of precipitation would then determine the morphology and integrity of the formed corrosion product, and consequently, the corrosion rate.

Our X-ray diffraction (XRD) data indicated significant surface roughening of the steel as the corrosion process proceeded, prior to the detection of carbonate layers [28]. The changes in the steel surface morphology are expected to play an important role in establishing critical boundary layer conditions for precipitation of corrosion product. In the present paper, we report the use of *in situ* synchrotron XRD to investigate the effects of steel microstructure in the development of a critical boundary layer, and on the nucleation and growth of iron carbonate. Three different steel microstructures and compositions were studied: pearlitic ferritic low carbon steel, quenched and tempered steels, and normalised steels (with and without chromium addition). The effects of mass transport conditions - controlling the supersaturation of iron carbonate by changing the CO_2 bubbling rate - and steel surface roughness, were also explored.

EXPERIMENTAL

Materials

Three different steel samples in the as-received condition and two heat treated steel samples were used in this study. The as-received steel samples were:

- AISI 1008 mild steel (labelled MS).
- API 5CT L80 pipeline steels:
    - Carbon steel without alloying element (labelled L80QT).
    - 1% Cr, 0.25% Mo low alloy steel (labelled 1Cr¼Mo L80QT).

The AISI 1008 mild steel sample had an equiaxed ferritic/pearlitic microstructure, typical of hot formed low carbon steel. The as-received API 5CT L80 pipeline steels (supplied by Tenaris) had a quenched and tempered martensitic microstructure, with high yield strength

and mechanical properties appropriate for well applications. The microstructures of the as-received steel samples are illustrated in Figure 1.

To study the effect of microstructure on CO_2 corrosion processes, the as-received API 5CT L80 pipeline steels were normalised in order to produce a ferritic/pearlitic microstructure. The heat treatment schedule included heating the L80QT and 1Cr¼Mo L80QT steel samples for 60 minutes at 880°C and 850°C respectively, followed by slow cooling in air to avoid the formation of bainite. The heat treated API 5CT L80 steel samples, having a ferritic/pearlitic microstructure with bands of pearlite (Figure 2) are labelled L80FP and 1Cr¼Mo L80FP. The steel compositions (obtained by optical emission spectroscopy) and hardness measurements are given in Table 1.

Table 1: Steel compositions (obtained by optical emission spectroscopy) and hardness measurement results.

Sample	Hardness (HV10)	Wt. % (and Fe bal.)										
		C	Si	Mn	Cr	Mo	S	P	Ni	Cu	Al	V
MS	141	0.06	0.04	0.30	0.05	<.01	0.019	0.012	0.06	0.16	<.01	<.01
L80QT	242	0.25	0.20	0.9	0.07	0.03	0.005	0.014	0.06	0.14	0.01	<.01
L80FP	168											
1Cr¼Mo L80QT	229	0.25	0.09	0.33	0.91	0.26	0.005	0.013	0.04	0.06	<.01	<.01
1Cr¼Mo L80FP	159											

Note: QT denotes quenched and tempered steel.
FP denotes ferritic pearlitic steel.

Synchrotron and Corrosion Experiments

In situ synchrotron XRD experiments were conducted at the Powder Diffraction beam line at the Australian Synchrotron, using an electrochemical cell with heating ability. The synchrotron cell allows XRD patterns to be recorded in real time while the sample is under electrochemical control in the test solution.

Details of the cell designed for these experiments have been given previously [28]. The cell comprises a reservoir into which the counter and reference electrodes are placed, with a tapering neck down to the working electrode. The working electrode (sample) is a 1.5 mm diameter rod of the material of interest, embedded in epoxy resin with the top face polished to 1 μm unless otherwise stated. Different roughness surface finishes obtained by abrading the surface with different grit size emery paper, were used to explore the effect of this parameter. A Pt counter electrode and Ag/AgCl (3M KCl) microreference electrode were used. The X-ray beam energy was 15 keV (i.e. λ = 0.82400 Å) and the beam size was 0.2 mm × 0.7 mm (vertical × horizontal). Diffraction images were recorded using a MarCCD 165 detector (apparent pixel size 79 μm) located 137 mm from the sample. The exposure

time for each image during the *in situ* measurements was 1 minute, with 3-4 seconds readout time. X-rays were incident on the polished surface of the sample rod at a grazing angle (< 1°).

The basic test solution used in this work was 0.5 M NaCl, CO_2-saturated by bubbling a stream of CO_2 gas at 1 bar, heated to 80 ± 1°C. A small volume of 2 M aqueous sodium hydroxide (NaOH) in 1:50 volume ratio was added to give a calculated pH at 80°C of 6.8. This solution had a measured pH of 6.2 at room temperature. The cell was sealed to prevent oxygen and other atmospheric contamination, and CO_2 was bubbled continuously throughout the experiment.

The corrosion process was accelerated through anodic polarization under potentiostatic control and the resulting current was recorded for up to 2 hours. Current densities in the following results are expressed with respect to the projected area of the specimen and do not take into account the non-uniform distribution of current across the specimen surface or the effects of changing surface roughness during the experiment. At the end of each experiment the solution was removed, the sample dried, and a 5 minute XRD exposure recorded using the same geometry, in order to analyse the pattern for minority phases which may be obscured by the solution scattering. The samples were then retained and stored in a dry environment for scanning electron microscopy (SEM) analysis, which was performed using a SEM Quanta 450.

Analysis of XRD data

The X-ray diffraction data were processed as described in the previous work [28]. All diffraction rings for all samples were isotropic. Fit2D was used to radially integrate the data, yielding 1D plots of intensity vs. 2θ. The most intense peak for each phase was fitted using a Gaussian peak function and the position, width, and peak area were recorded. This approach was deemed to be more robust than fitting the complete pattern, as due to the sample geometry the peak widths and intensities vary considerably with 2θ and generally do not match those expected for a powder pattern. Often only a few peaks of each phase can be observed in the *in situ* data, particularly at the early stages of scale formation. As an example, selected X-ray diffraction patterns recorded *in situ* during the experiment for L80FP steel are shown in Figure 3. In addition the peaks are broadened due to the size of the beam footprint (spilling over the whole sample) and the lack of post-sample collimation, so that accurate values of grain sizes cannot be determined from peak width analysis. By monitoring the peak area as a function of time, the relative kinetic information of the formation of these crystalline phases can be obtained. The integrated diffraction intensity (peak area) is linearly

proportional to the volume of the diffracting material, although absolute values of the film thickness cannot be extracted. It is difficult to obtain absolute growth rates to compare one sample to another due to the incidence angle being ill-defined. This means that the X-ray penetration depth, and hence the total volume of diffracting material, is unknown. Instead, the diffraction peak areas are normalised to the initial Fe signal to offset any incidence angle and illuminated area affects. The diffraction peak areas obtained are divided by the structure factor for that phase and reflection to give approximate relative volumes of material.

The X-ray diffraction patterns of the Fe (110) reflection were also analysed using statistical methods to characterise the changes in the iron diffraction pattern. Details on the statistical measures are described in [31]. The fractal dimension can be used as a measure of the smoothness of the diffraction ring. The development of 'spottiness' of the diffraction rings can be interpreted as the preferential dissolution of small grains, leaving behind larger grains which are insufficient in number to give a 'powder average' smooth diffraction ring [31]. The physical morphology of such a sample would be a roughened surface. Therefore increased 'spottiness' (as measured by fractal dimension) corresponds to increasing roughness of the steel surface. A fractal dimension of 2.0 indicates a smooth diffraction ring, and increases with increasing 'spottiness'. It is important to note the distinction between the 'spottiness' of the diffraction ring and the topological surface roughness of the sample – although in the case of preferential dissolution the two effects are indirectly related, the spots in the diffraction ring arise from the presence of distinct grains, not from the sample surface per se.

RESULTS

Plain Carbon Steel – Microstructural Variation

To study the effect of microstructure on corrosion processes, experiments were conducted on the as-received API 5CT L80 sample with a quenched and tempered microstructure (L80QT) and the heat treated sample having pearlitic ferritic microstructure (L80FP). Figure 4a shows the anodic current density of these steels in potentiostatic tests in 0.5 M NaCl solution at an applied potential of -500 mV (vs. Ag/AgCl, 3M KCl, or around 200 mV above the rest potential) and at 80°C. Figure 4b shows the relative volumes for each crystalline phase calculated from the *in situ* XRD data and Figure 4c shows the fractal dimension of the Fe (110) diffraction ring over the same time period. Note that the diffraction peak areas of each compound were normalised to the initial iron peak area to allow comparison of sequential tests.

As in the previous reports [29, 30], both of the samples showed a current density that was at first constant, then rose, then fell steeply to a low value. The rise in current density corresponds to the nucleation and spreading over the surface of a siderite layer and the drop corresponds to the approach towards full surface coverage by an impermeable layer. However, the shape of the observed current density peak, kinetics of corrosion product formation and the extent of surface roughening were significantly different for the two steel samples.

The normalised L80FP sample had a shorter induction time period, where the current density was relatively constant and no siderite layer was observed. The current density peak was also higher and sharper compared to the as-received quenched and tempered sample (L80QT), indicating faster formation of a protective layer. For example, time to reach maximum current density was around 15 minutes for the L80FP sample and 45 minutes for the L80QT sample. Chukanovite ($Fe_2(OH)_2CO_3$) was detected in both samples, arising after the formation of siderite. Chukanovite nucleated earlier for the L80FP sample and became the major phase detected. Cementite was also detected in these samples and was more pronounced in the quenched and tempered sample.

Figure 4c shows the fractal dimension of the Fe (110) diffraction ring from the X-ray diffraction pattern. The fractal dimension of the L80FP sample increased significantly during the induction period, and then diminished slightly once the corrosion product was formed. The fractal dimension of the Fe (110) diffraction ring for the L80FP sample increased from 2.08 to 2.21, indicating significant dissolution of small grains (and hence significant surface roughening) as the corrosion progressed. It then plateaued at the onset of passivation (around 20 minutes). Such behaviour was not observed to the same degree in the quenched and tempered sample. The fractal dimension for L80QT increased from 2.00 initially to a maximum of 2.03 and plateaued well before passivation.

Chromium/Molybdenum Containing Steel– Microstructural Variation

The effects of alloying elements in the steel composition on the corrosion mechanism in CO_2 environment were explored in our previous paper [30]. Figure 5 shows the effect of changing steel microstructures on chromium/molybdenum containing steels. The as-received quenched and tempered steel (1Cr¼MoL80QT) had a low initial current density and readily formed siderite to form a thin layer over the steel surface, causing the observed current density to fall to a low level. Figure 5a shows that the normalised steel sample (1Cr¼MoL80FP) did not have any significant differences in the current density transient.

The kinetics of siderite formation was similar for both steel samples to around 60 minutes; then for the 1Cr¼MoL80FP sample the growth rate decreased (Figure 5b).

Figure 5c shows that the normalised 1Cr¼MoL80FP sample had a gradual increase of the steel surface roughness as corrosion progressed, as indicated by an increase of the fractal dimension of the Fe (110) diffraction ring from 2.03 to 2.18. Similar to the plain carbon steel sample, such behaviour was not observed to the same degree for the quenched and tempered 1Cr¼MoL80QT sample: the steel did not significantly roughen according to the fractal dimension.

Surface Roughness Effect

Figure 6 shows the effect on CO_2 corrosion processes of mechanically changing the steel surface roughness. Two surface finishes on the mild steel sample were investigated: the standard 1 μm and a 320 Grit (particle size 46 μm) surface finish, labelled MS 1μm and MS 46μm respectively. The effect of pre-roughening the surface on the kinetics of siderite formation was dramatic. The current density rose immediately upon application of the anodic potential, without the induction time observed for the smooth surface, Figure 6a. An increased surface roughness also altered the nucleation and growth kinetics of both siderite and chukanovite phases. On the rough surface (46μm), siderite was detected very soon after application of the current and the layer grew rapidly. Chukanovite formed later and grew more slowly. On the polished surface (1μm), siderite nucleated first, when the induction time before the current rose was over, followed shortly after by chukanovite which then grew more rapidly, Figure 6b. Both steel samples showed increasing fractal dimension of the Fe diffraction ring until the current density peak was achieved, after which it plateaued, Figure 6c. The sample with a smooth surface showed a significant increase in the fractal dimension during the induction period, before the current density started to rise and siderite started to form (i.e. during the first 20 minutes). This shows that a roughened surface is required for siderite to form, either via mechanical or corrosion-related means. The increase of fractal dimension for the pre-roughened sample shows this also exhibits preferential dissolution of small grains, even while siderite is being deposited.

Stirring Effect: Change of Bubble Rate

In the synchrotron cell, a systematic and controlled variation of solution flow rate was not possible. We explored qualitatively the effect of stirring in the solution by altering the CO_2 gas bubbling rate. Three CO_2 gas flow rates were investigated: a standard case (~20 cm^3/s), a high flow rate (~40 cm^3/s) and a gas blanket system where the CO_2 inlet was positioned above the solution interface. The effect is shown in Figure7. Variation of the CO_2 gas flow

rate had a significant effect on the maximum current density observed as well as the induction time for precipitation. The peak current density increased with increase of stirring rate. The induction period was similar for the two flow experiments and but delayed for the gas blanket experiment. It is interesting to note that kinetics and relative volumes of siderite (filled symbols) were similar in all cases, but the amount of chukanovite formed (open symbols) varies. Chukanovite ultimately became the dominant phase in all three cases, Figure 7b.

Carbon Content Variation

Figure 8 shows the effect of changing steel carbon content on CO_2 corrosion by comparing the results for L80FP (having 0.25 Wt. % C) and MS (having 0.06 Wt. % C); note that both samples have a pearlitic ferritic microstructure. Higher carbon content resulted in a reduced induction period and slightly higher maximum current density. Following the induction period, siderite grew at a faster rate for the L80FP sample (with higher carbon content) compared to that observed for the MS sample. Chukanovite growth rate were similar in both cases and again ultimately became the dominant phase.

Morphology of Surface Layers

Selected SEM images of the formed surface layers and cross sectional views are shown in Figures 9 to 12. A thick layer of deposit was observed for the L80QT steel exposed at 80°C. The surface layer had two types of structures: small feathery plate-like structure and dense faceted nodules, Figure 9a, with thickness of around 18 μm (Figure 9b). A thinner deposit was observed on the normalised L80FP sample with thin plates at the film-steel interface, indicating remnants of cementite in the pearlite phase, Figure 9d. The surface morphology showed similar small plate-like structures with the absence of dense nodular crystal growth (Figure 9c).

For the chromium and molybdenum containing steels (1Cr¼MoL80QTand 1Cr¼MoL80FP), siderite readily formed on the steel surface and grew at a lower rate than on the non-Cr steels. These steels showed a dense surface layer of siderite but also showed some evidence of the development of localised corrosion, Figure 10. The as-received sample, 1Cr¼MoL80QT, had a thin smooth corrosion product layer up to 6 μm in thickness. Despite the low observed corrosion current density, the 1Cr¼MoL80QT steel showed some localised open areas where shallow pitting was observed, Figure 10a. Although both steel samples had similar overall average siderite growth rate, there was a significant difference in the distribution of thickness of the scale across different parts of the structure, revealed by the cross-sectional micrographs. For the ferritic-pearlitic microstructure, the cross-section after

the experiment showed significant roughening with the corrosion product deposited mainly into grooves etched into the surface, whose size scale is consistent with the initial microstructure; this observed roughening (Figure 10d) was consistent with the roughening deduced from the diffraction experiment, Figure 5c. There was some evidence of attack along grain boundaries in the steel.

Variation of surface morphology with variation of surface roughness and gas transport rates on mild steel samples is illustrated in Figures 11 and 12. Increased surface roughness promoted the formation of nodules over a small platelet structure (see Figure 11a *vs.* Figure 11b. A thicker and more adherent deposit was also observed for the roughened surface, see Figure 11d. Small platelets overlying a thick, dense surface layer were formed from the rapidly bubbled solution (Figure 12a) whilst the deposit from the unstirred solution showed larger crystals (Figure 12b).

DISCUSSION

It is evident that each of the variables – microstructure, surface roughness and stirring – had a critical effect on the nucleation, growth and final morphology of the protective surface scales of siderite and chukanovite. These effects can be rationalised in terms of the requirement to develop a critical supersaturation, the local pH changes that accompany the rapid nucleation and growth of siderite, and the effect of surface roughness (which alters as corrosion progresses in a fashion dependent on the microstructure) on the evolution over time of the solution composition near the interface.

The normalised steel sample having ferritic pearlitic microstructure showed increasing fractal dimension of the Fe(110) diffraction ring as corrosion progresses, indicating preferential dissolution of small grains. This observation, combined with the increasing relative volume of cementite phase detected in the *in situ* diffraction result, supports the theory of preferential dissolution of the ferrite phase. Remnants of cementite layers (see Figure 9d and Figure 10d) were also observed in the cross section and were detected in the diffraction pattern. The roles of cementite phase in the formation of a protective layer have been the subject of several studies [1, 2, 5-9]. Under certain conditions, siderite and cementite can form an adherent layer with the cementite phase acting as a framework for the scale growth. The synchrotron experiment showed that protective layer was formed at a much faster rate on the ferritic pearlitic sample (L80FT) in comparison with the quenched and tempered sample (L80QT). The propensity of ferritic pearlitic samples to develop significant surface roughness in comparison to the quenched and tempered samples was shown to reduce the required

induction time to reach local critical supersaturation, increased the rate of precipitation and increased the amount of chukanovite phase formed.

Comparing the XRD results for plain carbon steel, either mechanically pre-roughened or with varying CO_2 flow rates, with the surface morphology observed by SEM implies that the feathery plate-like structures correspond to chukanovite. The increase of chukanovite phase in the XRD corresponds to an apparent increase in the amount of the plate-like structure observed in the surface microstructure, although it should be noted that the volume or thickness of the various phases cannot be determined using the SEM. A needle or plate-like morphology associated with chukanovite is consistent with microscopy of the authentic mineral [32]. In the cross-sectional SEM images, the feathery plate morphology appeared to be on the outside of the scale, consistent with chukanovite forming later than siderite. The results of this study suggest that siderite crystals act as nuclei for the formation of chukanovite. The formation of chukanovite appears to be connected to the rate of precipitation of siderite and to the rate of increase of the current.

Table 2 shows the final approximate ratios of chukanovite to siderite and cementite to siderite ratio for all tested conditions. There appear to be a correlation between the CO_2 transport rate and the surface roughness on the resulting phases being formed. Stirring the solution (in comparison with the gas blanket system) resulted in increased amount of chukanovite phase being formed. The growth rate (and passivation) of siderite affects growth of chukanovite. For the roughened surface, where siderite growth rates were very high, only low levels of chukanovite were detected. It was previously hypothesised that the increase of current is connected to the decrease of local pH, in turn connected to the consumption of CO_2 by precipitation of siderite and to the transport rate of CO_2 from the solution to the interface [29]. The formation of chukanovite is also suggested to be sensitive to the local pH conditions around the surface of the siderite crystals.

Table 2: Approximate steady state volume ratio of various phases formed during CO_2 corrosion.

Sample	Conditions	Chukanovite : Siderite Ratio	Cementite : Siderite Ratio
L80	Ferritic pearlitic	1.89	0.20
	Quenched tempered	0.73	0.05
1Cr1/4MoL80	Ferritic pearlitic	N/A**	0.30
	Quenched tempered	N/A**	0.39
Mild Steel	Roughened surface	0.40	N/A***
	Standard conditions*	3.77	N/A***
	High bubble rate	3.09	N/A***
	Gas blanket system	1.87	N/A***

Note: * Standard conditions = fine surface, standard CO_2 bubble rate.
** Chukanovite was not detected.
*** Cementite was not detected.

Studies on the factors and conditions controlling the formation of chukanovite are limited. A number of research studies conducted under room temperature suggested that the formation of chukanovite is largely dependent on the ratio of dissolved iron concentration to carbonate and hydroxide species concentrations [33, 34]. The formation of chukanovite *vs.* siderite was shown to be sensitive to the rate of iron dissolution and solution pH [35]. Azoulay et al. [33] suggested that chukanovite is favoured to form in near neutral to alkaline pH (between 8 to 11) while siderite only formed at pH less than 6.5. A recent thermodynamic study of the formation of chukanovite suggested that chukanovite is metastable with respect to siderite at all pH and carbonate concentrations [36]. Tanusabrungsun et al. [37] also reported a transformation of chukanovite (associated with a plate-like structure) to siderite (associated with a cubic structure) during a 30 day coupon exposure trial in CO_2 saturated condition at temperatures of up to 150°C. However, others [14] have reported a reduction in corrosion rates for carbon steel exposed to CO_2 environment at temperatures above 60°C due to the formation of a more protective iron hydroxycarbonate scale. Whether the formation of the small plate-like morphology that we have tentatively associated with chukanovite is significant for the corrosion-protective properties of the scale is still an open question.

We have previously shown that for the chromium and molybdenum containing steels (1Cr¼MoL80QTand 1Cr¼MoL80FP), the critical effect is that of chromium in solution (derived from dissolution of the metal) on the nucleation of siderite and have noted from *ex situ* measurements that chromium is incorporated into the scale [30]. We suggest that different microstructures lead to different local concentrations of chromium in the solution, because the different phases in the steel (i.e. cementite and ferrite) have different concentration of chromium and dissolve at different rates. Hence it is speculated that microstructure-dependent spatial variations in the concentration of chromium in the solution

could lead to large local variations in the rate of precipitation of siderite and hence amplify effects of spatial variation of dissolution rate of the steel.

This work illustrates that microstructures that promote an early achievement of critical supersaturation and that promote mechanical attachment of the scale should be advantageous for the formation of a protective siderite scale. Although it has not been considered here, we also note that, for corrosion at open circuit, the spatial distribution of the cathodic reaction will also be of importance, since that will be another factor controlling the local pH. Microstructure, particularly the form and spatial distribution of cementite, should be of great importance in this respect.

CONCLUSIONS

1. Surface roughness, its development as a consequence of corrosion, and the resultant dependence on microstructure of the steel, is of great importance in influencing the protectiveness of siderite scales formed during CO_2 corrosion.
2. Local conditions determined by surface roughness and transport of solution species, and the interplay between precipitation rate of siderite and local pH changes determine the subsequent nucleation and growth of chukanovite, which could be speculated to have an important effect on the scale morphology and consequent corrosion protection.
3. The presence of Cr in the alloy is particularly important in determining the nucleation and growth of siderite. For Cr-containing steels, there may be a microstructure-dependent early development of localised corrosion under CO_2 conditions that may be sensitive to local chromium concentration in solution and may be related to spatial segregation of Cr between different phases of the alloy.

ACKNOWLEDGEMENTS

This work was funded by the New Zealand Ministry of Business, Innovation and Employment under contract C08X1003. Portions of this research were undertaken on the Powder Diffraction beam line at the Australian Synchrotron, Victoria, Australia. We thank the New Zealand Synchrotron Group Ltd. for a grant to construct the electrochemical cell. Thanks also to Nick Birbilis (Monash University) for his generous advice and loan of equipment and to Tenaris for the supply of steel samples.

REFERENCES

[1] M.B. Kermani, A. Morshed, Carbon Dioxide Corrosion in Oil and Gas Production—A Compendium, Corrosion, 59 (2003) 659-683.
[2] S. Nesic, L. Lunde, Carbon Dioxide Corrosion of Carbon Steel in Two-Phase Flow, Corrosion, 50 (1994) 717-727.
[3] A. Dugstad, H. Hemmer, M. Seiersten, Effect of steel microstructure upon corrosion rate and protective iron carbonate film formation., in: CORROSION/2000, NACE International, Paper No. 00024, 2000.
[4] D.A. Lopez, T. Perez, S.N. Simison, The influence of microstructure and chemical composition of carbon and low alloy steels in CO_2 corrosion. A state-of-the-art appraisal, Materials & Design, 24 (2003) 561-575.
[5] J.L. Crolet, N. Thevenot, S. Nesic, Role of Conductive Corrosion Product in the Protectiveness of Corrosion Layers, Corrosion, 54 (1998) 194-203.
[6] J.L. Mora-Mendoza, S. Turgoose, Fe_3C influence on the corrosion rate of mild steel in aqueous CO_2 systems under turbulent flow conditions, Corrosion Science, 44 (2002) 1223-1246.
[7] M. Ueda, H. Takabe, Effect of Environmental Factor and Microstructure on Morphology of Corrosion Products in CO_2 Environments, in: CORROSION/99, NACE International, Paper No. 13, 1999.
[8] M. Ueda, A. Ikeda, Effect of Microstructure and Cr Content in Steel on CO_2 Corrosion, in: CORROSION/96, NACE International, Paper No. 13, 1996.
[9] C.A. Palacios, J.R. Shadley, Characteristics of Corrosion Scales on Steels in a CO_2-Saturated NaCl Brine, CORROSION, 47 (1991) 122-127.
[10] L. Paolinelli, T. Perez, S. Simison, The effect of pre-corrosion and steel microstructure on inhibitor performance in CO_2 corrosion, Corrosion Science, 50 (2008) 2456-2464.
[11] F. Farelas, B. Brown, S. Nesic, Iron Carbide and its Influence on the Formation of Protective Iron Carbonate in CO_2 Corrosion of Mild Steel, in: CORROSION/2013 Paper No. 2291, NACE International, 2013.
[12] D.R. Askeland, W.J. Wright, Electrochemical Corrosion, in: Essentials of Materials Science & Engineering, Global Engineering, 2014, pp. 625-650.
[13] L.D. Paolinelli, T. Pérez, S.N. Simison, The influence of steel microstructure, chemical composition and pre-corrosion on CO_2 corrosion inhibitor efficiency, in: CORROSION/07, NACE International, Paper no. 07311, 2007.
[14] S. Al-Hassan, B. Mishra, D.L. Olson, M.M. Salama, Effect of Microstructure on Corrosion of Steels in Aqueous Solutions Containing Carbon Dioxide, Corrosion, 54 (1998) 480-491.
[15] A. Dugstad, H. Hemmer, M. Seiersten, Effect of Steel Microstructure on Corrosion Rate and Protective Iron Carbonate Film Formation, Corrosion, 57 (2001) 369-378.
[16] E. Gulbrandsen, S. Nesic, A. Stangeland, T. Burchardt, B. Sundfaer, S.M. Hesjevik, S. Skjerve, Effect of Precorrosion on the Performance of Inhibitors for CO_2 Corrosion of Carbon Steel, in: Paper No. 13, CORROSION/98, NACE International, 1998.
[17] K. Denpo, H. Ogawa, Effects of nickel and chromium on corrosion rate of linepipe steel, Corrosion Science, 35 (1993) 285-288.
[18] A. Dugstad, L. Lunde, K. Videm, Parametric study of CO_2 corrosion of carbon steel, in: CORROSION 94, NACE, Paper No. 473, 1994.
[19] M. Kimura, Y. Saito, Y. Nakano, Effects of Alloying Elements on Corrosion Resistance of High Strength Linepipe Steel in Wet CO_2 Environment, in: Paper No. 18, CORROSION 94, NACE International, 1994.
[20] E.W.J.V. Hunnik, B.F.M. Pots, E.L.J.A. Hendriksen, The formation of protective $FeCO_3$ corrosion product layers in CO_2 corrosion, in: Paper No. 6, CORROSION/96, NACE International, 1996.

[21] G. Schmitt, M. Hörstemeier, Fundamental Aspects of CO_2 Metal Loss Corrosion Part II: Influence of Different Parameters on CO_2 Corrosion Mechanisms, in: CORROSION, Paper No. 06112, NACE International, 2006.
[22] A. Dugstad, Fundamental Aspects of CO_2 Metal Loss Corrosion Part I: Mechanism, in: CORROSION, Paper No. 06111, NACE International, 2006.
[23] S. Nesic, Key issues related to modelling of internal corrosion of oil and gas pipelines - A review, Corrosion Science, 49 (2007) 4308-4338.
[24] G. Schmitt, Fundamental Aspects of CO2 corrosion, in: Corrosion 1983 Symposium NACE - Advances in CO_2 Corrosion Volume 1, 1983.
[25] C.D. Waard, D.E. Milliams, Carbonic Acid Corrosion of Steel. Corrosion, Corrosion, 31 (1975) 177-181.
[26] R. Nyborg, CO_2 Corrosion Models for Oil and Gas Production Systems, in: Paper No. 10371, CORROSION/2010, NACE International, 2010.
[27] R. Nyborg, Overview of CO_2 Corrosion Models for Wells and Pipelines, in: Paper No. 02233, CORROSION/2002, NACE International, 2002.
[28] B. Ingham, M. Ko, G. Kear, P. Kappen, N. Laycock, J.A. Kimpton, D.E. Williams, In situ synchrotron X-ray diffraction study of surface scale formation during CO_2 corrosion of carbon steel at temperatures up to 90°C, Corrosion Science, 52 (2010) 3052-3061.
[29] B. Ingham, M. Ko, N. Laycock, J. Burnell, P. Kappen, J.A. Kimpton, D.E. Williams, In situ synchrotron X-ray diffraction study of scale formation during CO_2 corrosion of carbon steel in sodium and magnesium chloride solutions, Corrosion Science, 56 (2012) 96-104.
[30] M. Ko, B. Ingham, N. Laycock, D.E. Williams, In Situ Synchrotron X-Ray Diffraction Study Of The Effect Of Chromium Additions To The Steel And Solution On CO_2 Corrosion Of Pipeline Steels, Corrosion Science, 80 (2014) pp 237-246.
[31] B. Ingham, Statistical measures of spottiness in diffraction rings, Journal of Applied Crystallography, 47 (2014) 166-172.
[32] I.V. Pekov, N. Perchiazzi, S. Merlino, V.N. Kalachev, M. Merlini, A.E. Zadov, Chukanovite, $Fe_2(CO_3)(OH)_2$, a new mineral from the weathered iron meteorite Dronino, Eur. J. Mineral, 19 (2007) 891-898.
[33] I. Azoulay, C. Remazeilles, P. Refait, Determination of standard Gibbs free energy of formation of chukanovite and Pourbaix diagrams of iron in carbonated media, Corrosion Science, 58 (2012) 229-236.
[34] C. Rémazeilles, P. Refait, Fe(II) hydroxycarbonate $Fe_2(OH)_2CO_3$ (chukanovite) as iron corrosion product: Synthesis and study by Fourier Transform Infrared Spectroscopy, Polyhedron, 28 (2009) 749-756.
[35] J. Dong, T. Nishimura, T. Kodama, Corrosion Behaviour of Carbon Steel in Bicarbonate (HCO_3^-) Solutions, in: Mat. Res. Soc. Symp. Proc, 2002, pp. 105-112.
[36] P. Refait, J.A. Bourdoiseau, M. Jeannin, D.D. Nguyen, A. Romaine, S. Sabot, Electrochemical formation of carbonated corrosion products on carbon steel in deaerated solutions, Electrochimica Acta, 79 (2012) 210-217.
[37] T. Tanupabrungsun, D. Young, B. Brown, S. Nešić, Construction and Verification of Pourbaix Diagrams for CO_2 Corrosion of Mild Steel Valid up to 250°C, in: Paper no 1418, NACE/2012, NACE International, 2012.

FIGURES

Figure 1: Microstructures of as-received samples: (a) ferritic/pearlitic microstructure of MS sample; (b) and (c) quenched and tempered martensitic microstructure of the L80QT and 1Cr¼Mo L80QT steels, respectively.

Figure 2: Ferritic/pearlitic microstructure of the normalised API 5CT L80 steels: (a) L80FP; (b) 1Cr¼Mo L80FP.

Figure 3: Selected XRD patterns recorded in situ during the experiment for L80FP steel. Fe: steel. S: siderite, $FeCO_3$, C = chukanovite, $Fe_2(OH)_2CO_3$, * = cementite, Fe_3C and + = sodium chloride, NaCl. Arrows indicate the siderite and chukanovite peak areas used for analysis.

Figure 4: In situ synchrotron XRD results for potentiostatic tests of L80QT and L80FP steels at -500 mV (*vs*. Ag/AgCl 3M KCl) in CO_2 saturated 0.5 M NaCl solution at 80°C: (a) electrochemical current density; (b) approximate relative volumes for each phase; (c) fractal dimension of Fe(110) diffraction ring.

Figure 5: In situ synchrotron XRD results for potentiostatic tests of 1Cr¼MoL80QT and 1Cr¼MoL80FP steels at -500 mV (*vs*. Ag/AgCl 3M KCl) in CO_2 saturated 0.5 M NaCl solution at 80°C: (a) electrochemical current density; (b) approximate relative volumes for each phase; (c) fractal dimension of Fe(110) diffraction ring.

Figure 6: In situ synchrotron XRD results for potentiostatic tests of MS with 1 μm and 320 Grit (particle size 46 μm) surface finish at -500 mV (*vs*. Ag/AgCl 3M KCl) in CO_2 saturated 0.5 M NaCl solution at 80°C: (a) electrochemical current density; (b) approximate relative volumes for each phase; (c) fractal dimension of Fe(110) diffraction ring.

Figure 7: In situ synchrotron XRD results for potentiostatic tests of MS with varying CO_2 flow rates at -500 mV (*vs*. Ag/AgCl 3M KCl) in CO_2 saturated 0.5 M NaCl solution at 80°C: (a) electrochemical current density; (b) approximate relative volumes for each phase; (c) fractal dimension of Fe(110) diffraction ring.

Figure 8: In situ synchrotron XRD results for potentiostatic tests of MS (0.06% C) and L80FP (0.25% C) at -500 mV (*vs*. Ag/AgCl 3M KCl) in CO_2 saturated 0.5 M NaCl solution at 80°C: (a) electrochemical current density; (b) approximate relative volumes for each phase; (c) fractal dimension of Fe(110) diffraction ring.

Figure 9: SEM images of (a) and (b) surface morphology; (c) and (d) cross sectional views of scales formed at 80°C on L80QT and L80FP.

Figure 10: SEM images of (a) and (b) surface morphology; (c) and (d) cross sectional views of scales formed at 80°C on 1Cr¼MoL80QT and 1Cr¼MoL80FP.

Figure 11: SEM images of (a) and (b) surface morphology; (c) and (d) cross sectional views of scaled formed at 80°C on MS samples having 1μm and 46 μm surface finish.

Figure 12: SEM images of (a) and (b) surface morphology; (c) and (d) cross sectional views of scales formed at 80°C on MS samples with high CO_2 bubble rate (~40cm^3/s) and gas blanketing.

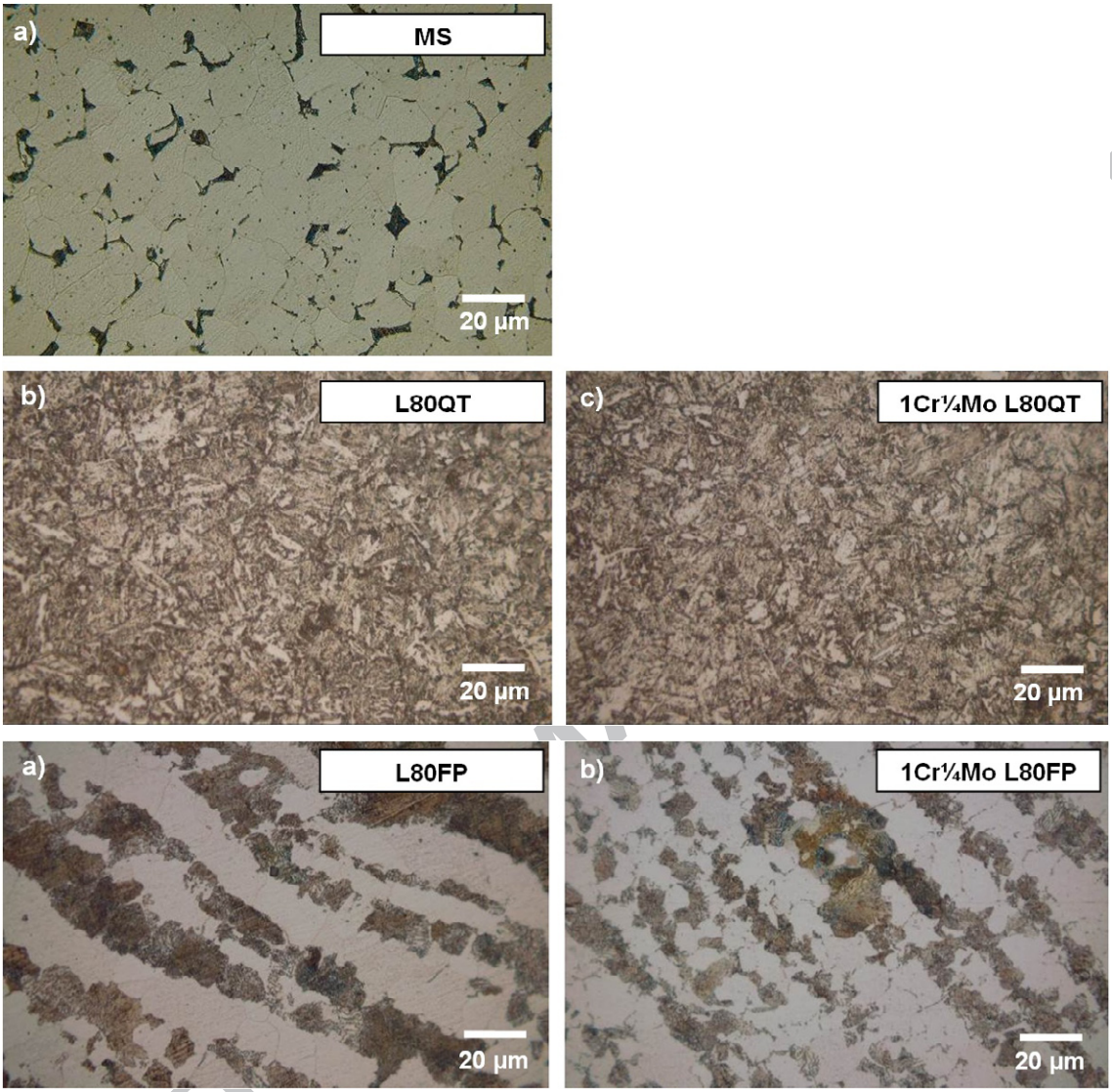

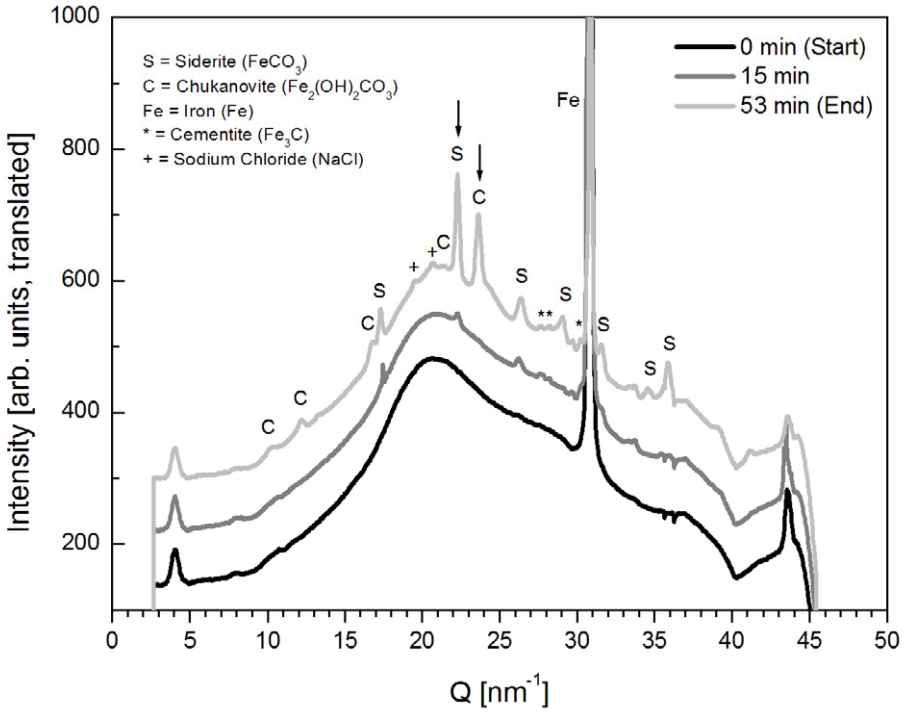

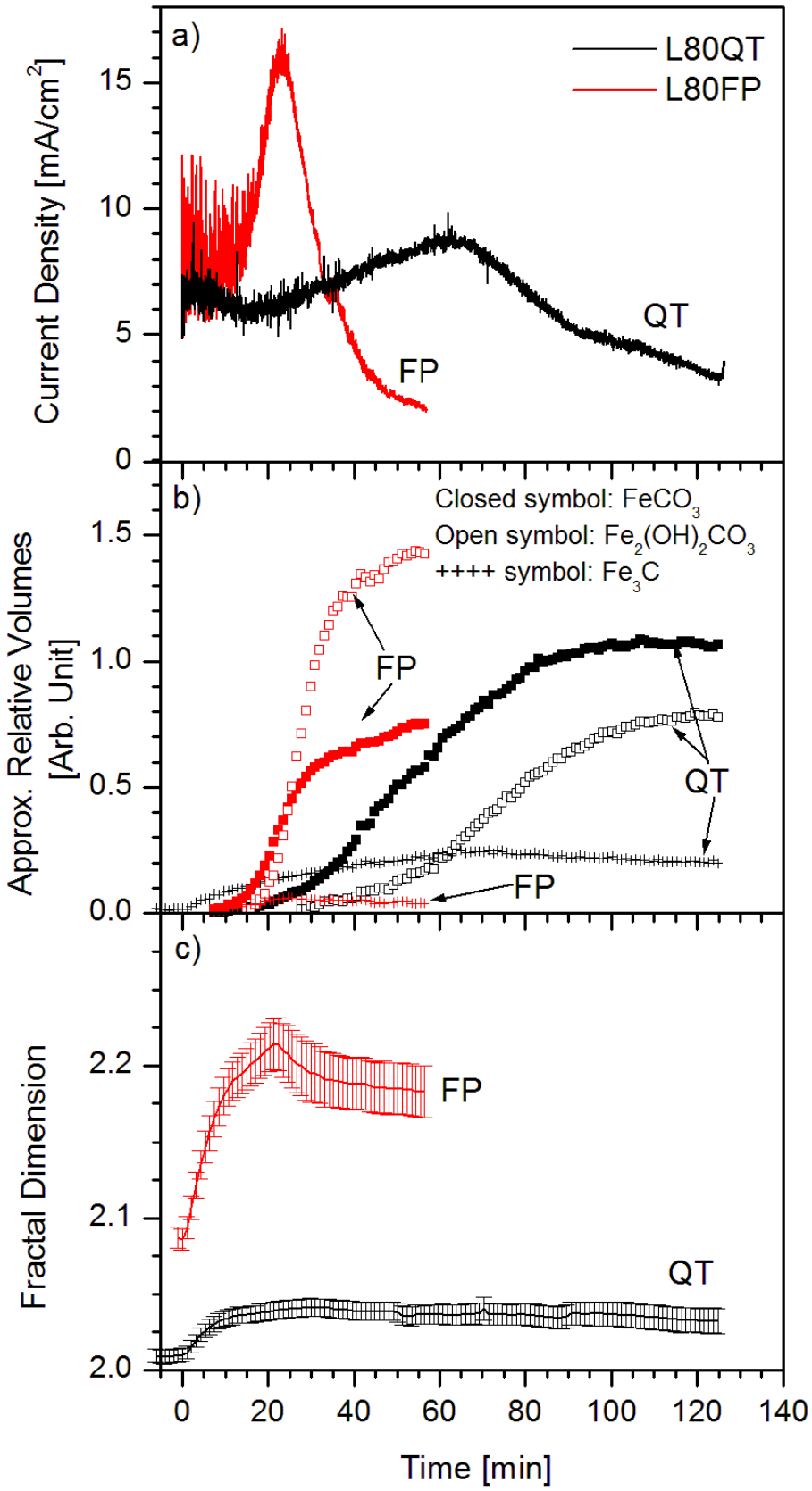

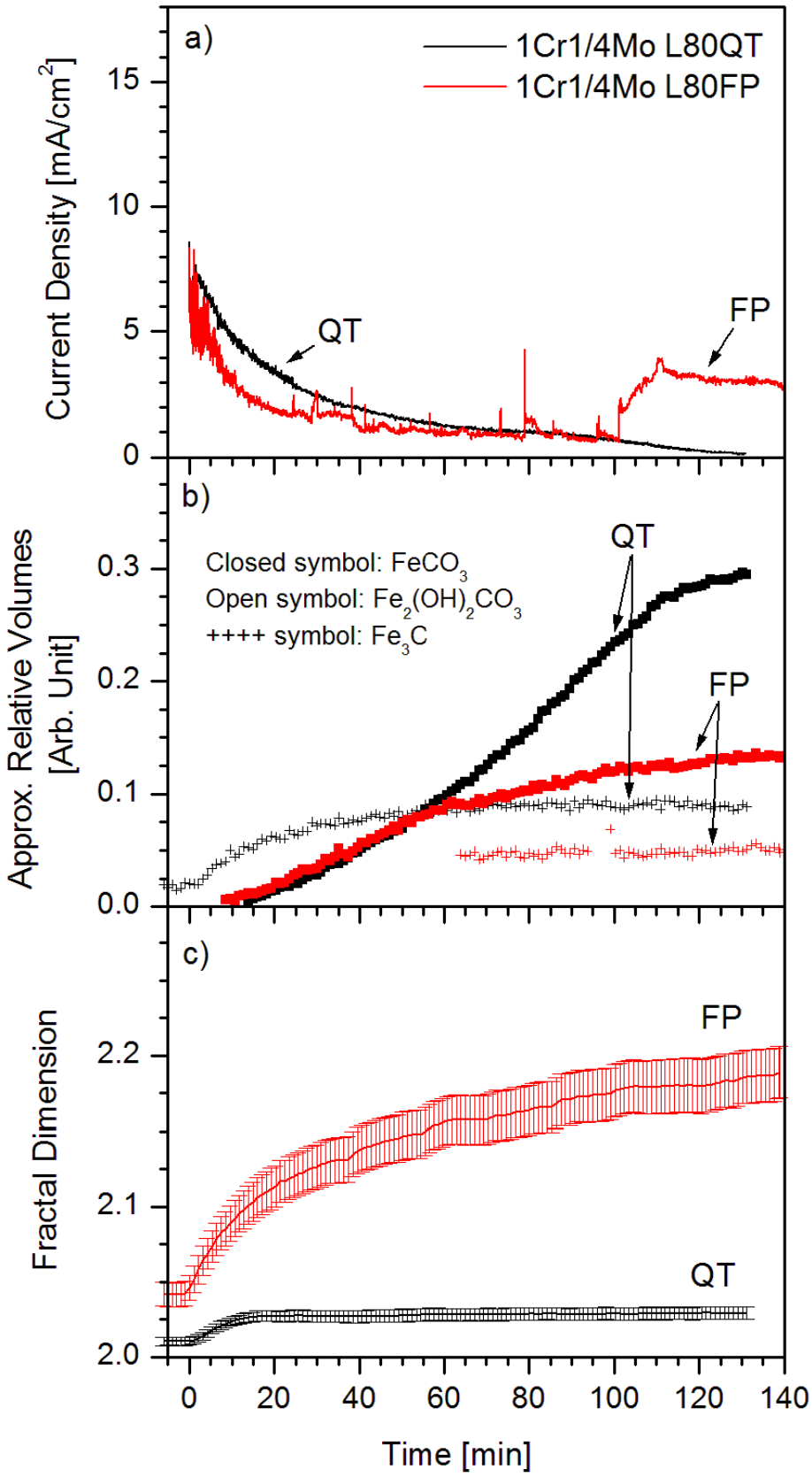

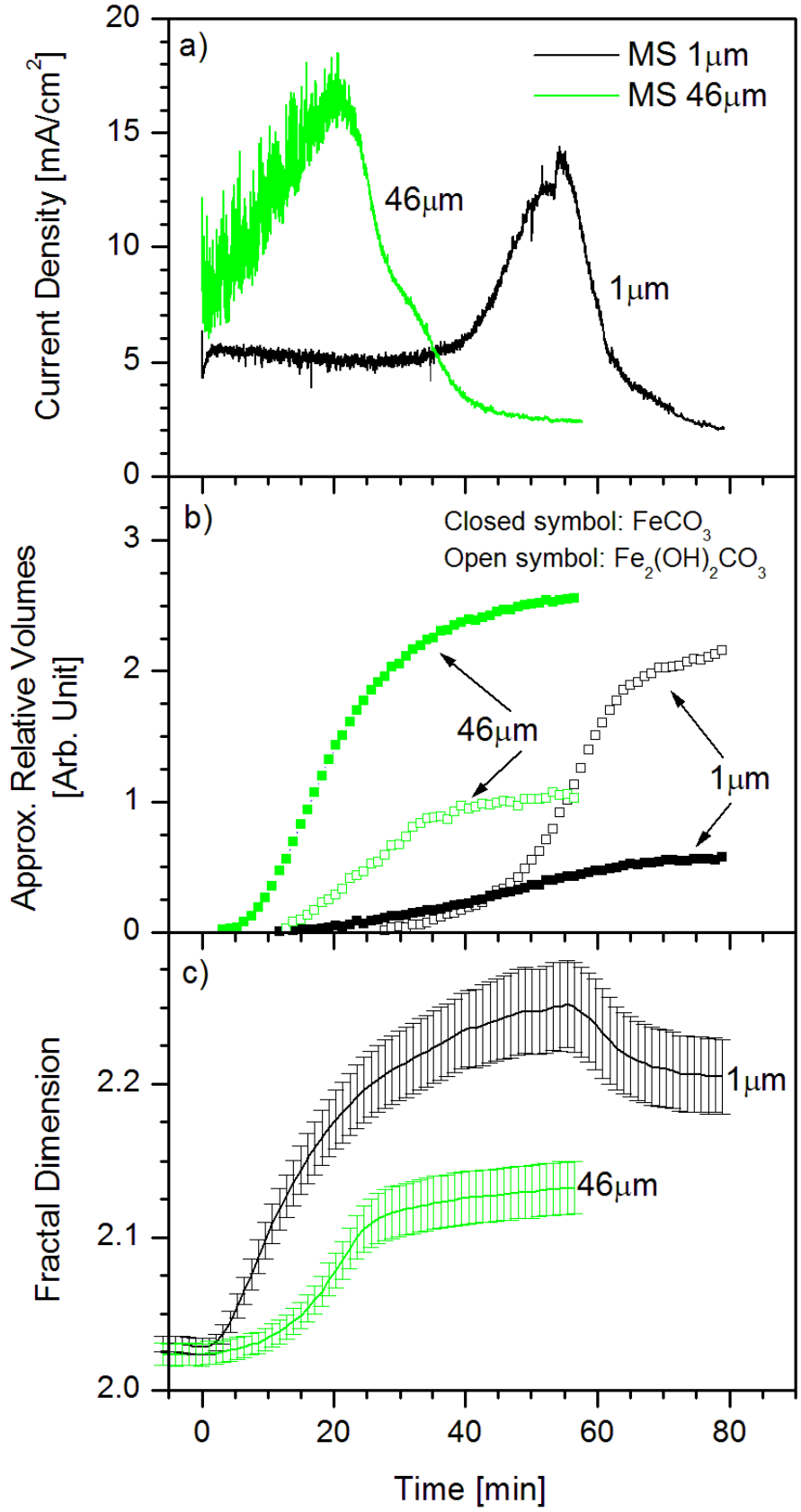

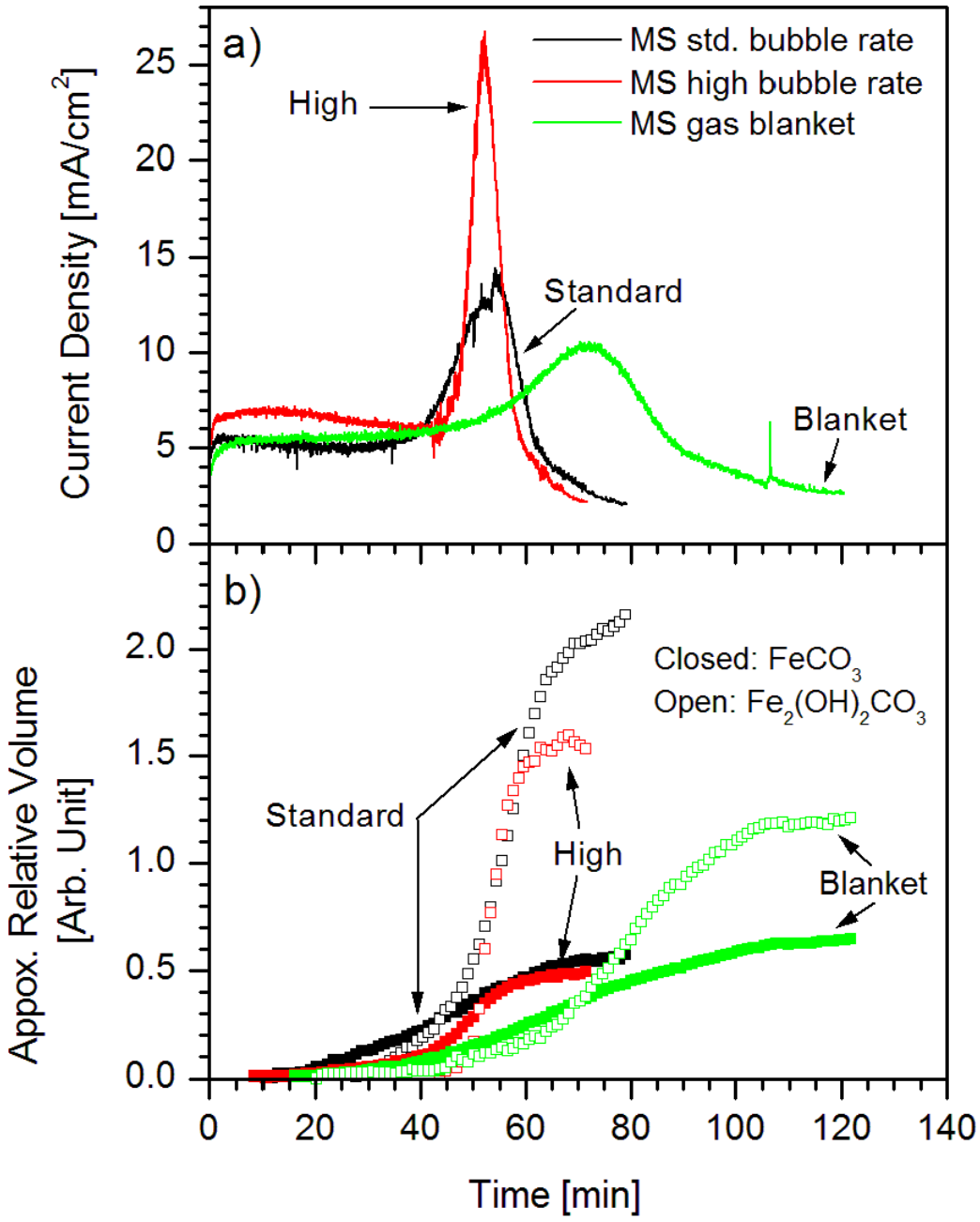

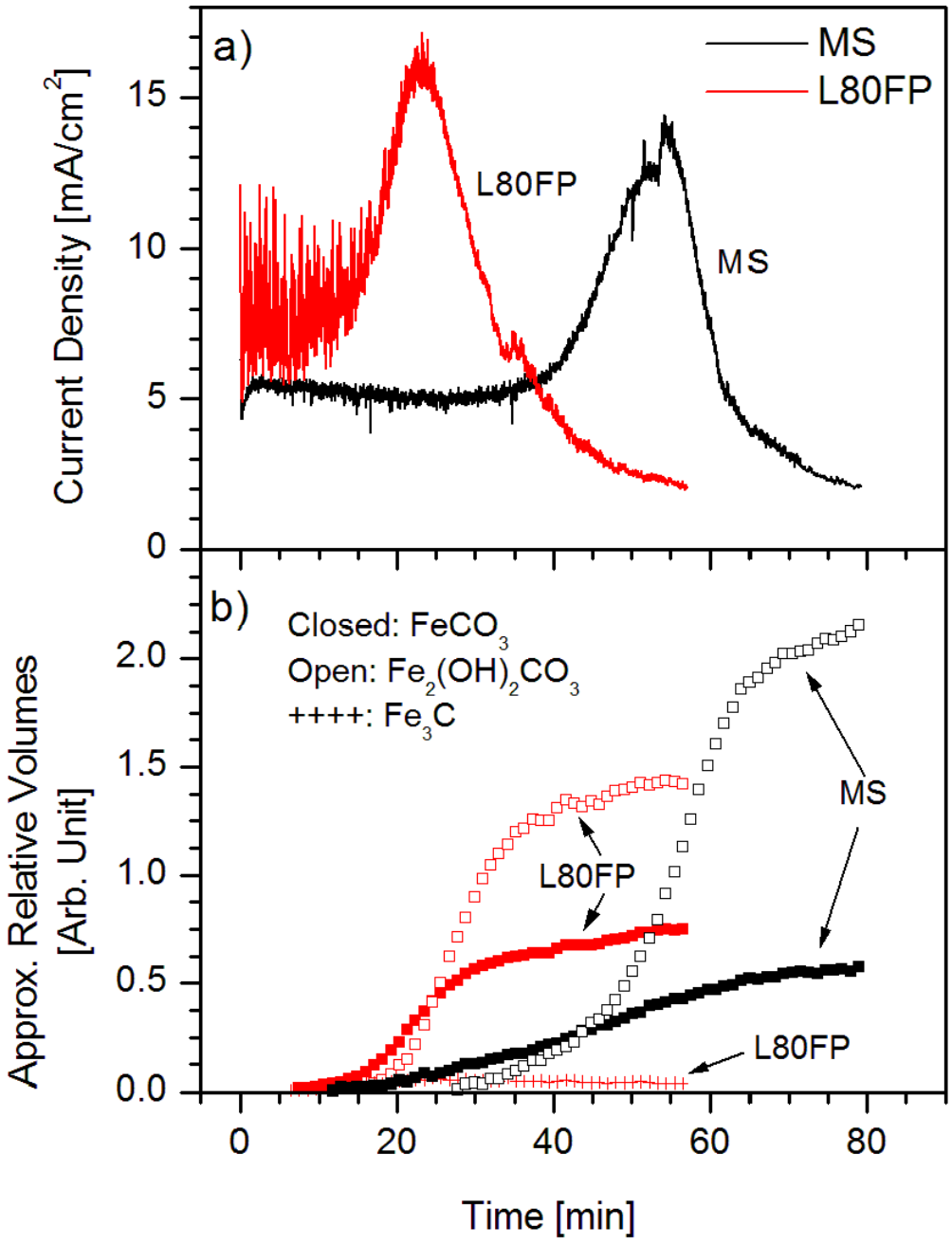

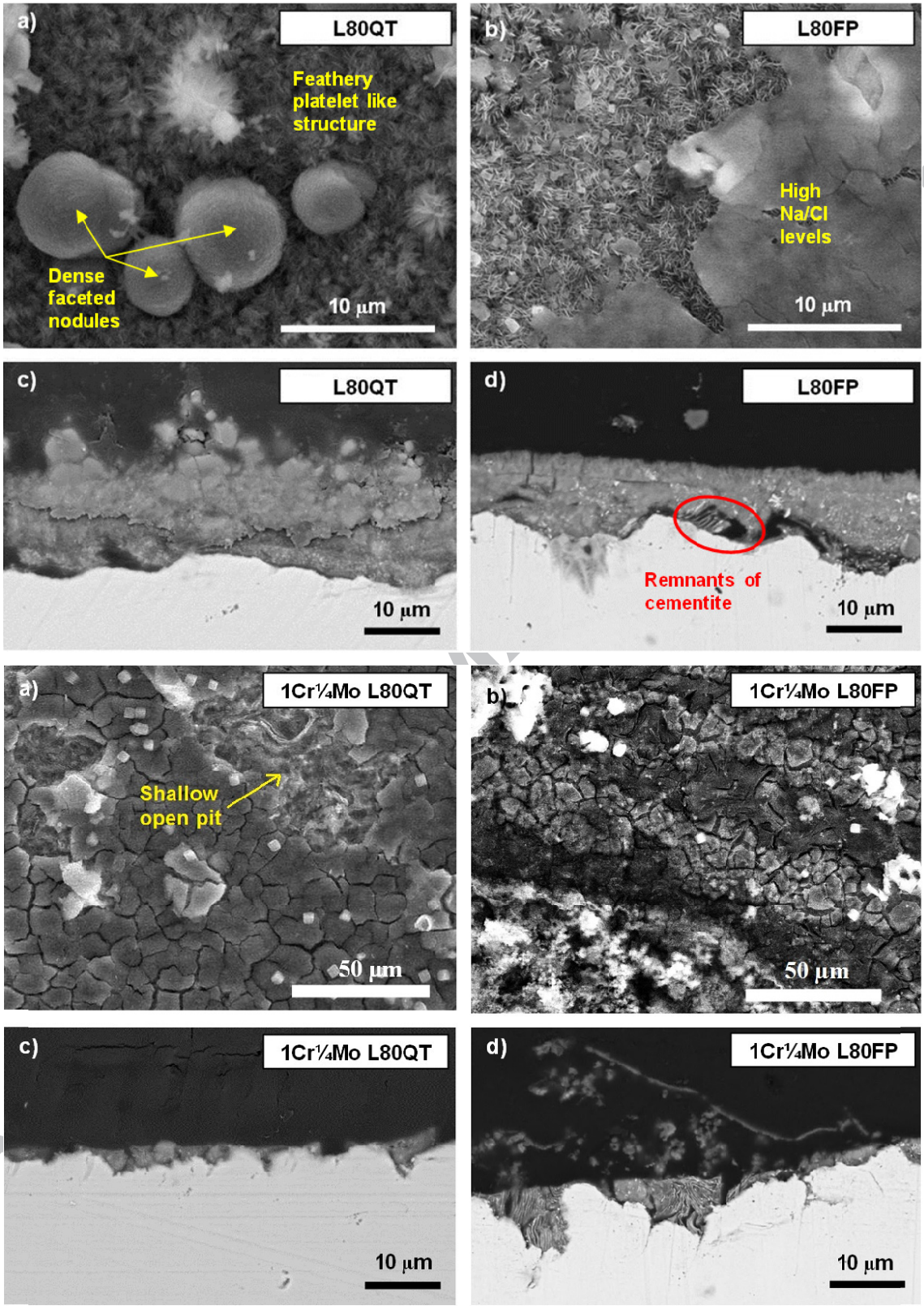

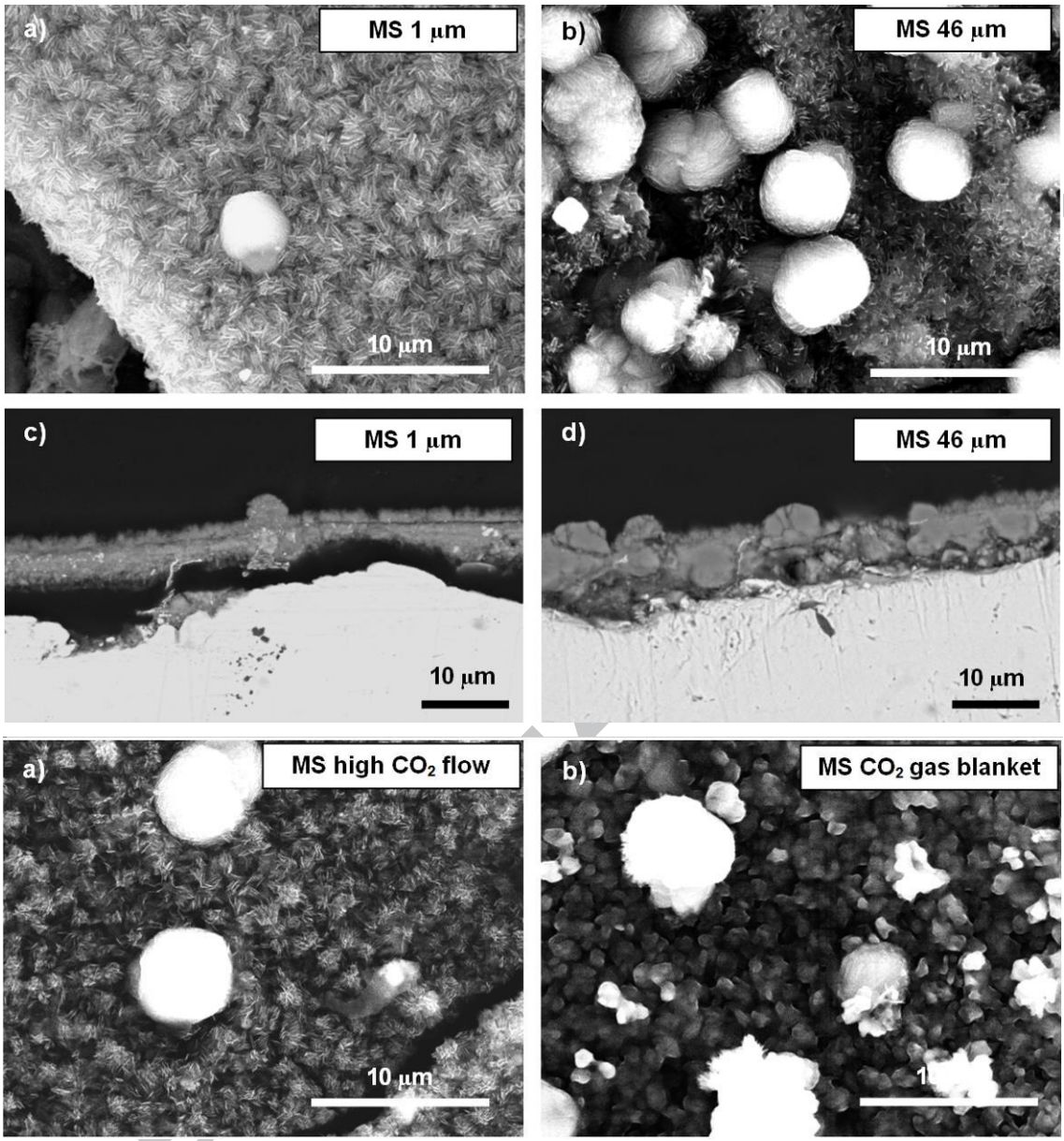

Highlights

> We studied the effects of steel microstructures and local conditions on CO_2 corrosion.

> Microstructure influences the development of surface roughness during corrosion.

> The effects of Cr alloying, on average, dominate over the effects of microstructure.

> Spatial segregation of Cr between the phases in the steel may result in localised corrosion.